



## Simple surface treatment improves performance of carbon materials for sodium ion battery anodes

Sergio Aina<sup>a</sup>, Blaz Tratnik<sup>b</sup>, Alen Vizintin<sup>b</sup>, Elena Tchernychova<sup>b</sup>, M. Pilar Lobera<sup>a,d</sup>, Robert Dominko<sup>b,c</sup>, María Bernechea<sup>a,d,e,\*</sup>

<sup>a</sup> Instituto de Nanociencia y Materiales de Aragón (INMA) CSIC-Universidad de Zaragoza, Department of Chemical and Environmental Engineering, University of Zaragoza, Campus Río Ebro-Edificio I+D, C/ Mariano Esquillor S/N, 50018, Zaragoza, Spain

<sup>b</sup> National Institute of Chemistry, Hajdrihova 19, SI 1001, Ljubljana, Slovenia

<sup>c</sup> Faculty of Chemistry and Chemical Technology, University of Ljubljana, Večna pot 113, 1000, Ljubljana, Slovenia

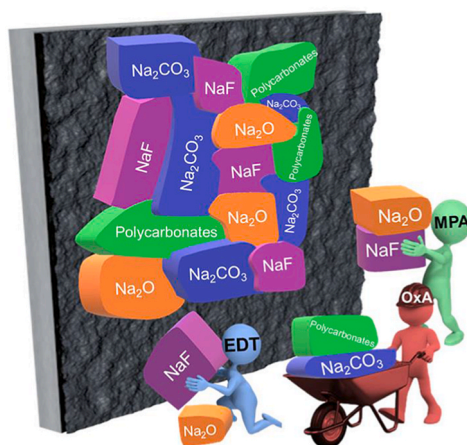
<sup>d</sup> Centro de Investigación Biomédica en Red de Bioingeniería, Biomateriales y Nanomedicina, Instituto de Salud Carlos III, 50018, Zaragoza, Spain

<sup>e</sup> ARAID, Government of Aragón, 50018, Zaragoza, Spain

### HIGHLIGHTS

- Hard carbons are the most extended anode materials for sodium-ion batteries (SIBs); however, they show some limitations.
- A simple, fast, low-cost treatment with small molecules blocks micropores, improves Na diffusion and increases capacity.
- *Ex-situ* XPS demonstrates that thiol functional groups promote the formation of a favorable solid electrolyte interface.
- The treatment improves performance of soft carbons as well, demonstrating the wide applicability of the method.

### GRAPHICAL ABSTRACT



### ABSTRACT

Hard carbons are the most extended anode materials for sodium-ion batteries (SIBs); however, they suffer from several limitations such as low stability, poor rate performance and low initial Coulombic efficiency (iCE). Herein, a simple, fast, and low-cost surface treatment at room temperature using short-chain organic molecules: 3-mercaptopropionic acid (MPA), 1,2-ethanedithiol (EDT) and oxalic acid (OxA) has been applied to a hard carbon (C1400).

The carbons treated with sulfur containing molecules (MPA or EDT) exhibit higher capacity (12 % capacity enhancement after 100th cycles at C/10 and 18 % enhancement at 1C vs. C1400). The introduction of these ligands leads to improved micropore blockage, helping in the reversible insertion of Na ions. Moreover, *ex-situ* X-ray photoelectron spectroscopy (XPS) analyses demonstrate that thiol functional groups promote the formation of favorable NaF and Na<sub>2</sub>O-rich solid electrolyte

\* Corresponding author. Instituto de Nanociencia y Materiales de Aragón (INMA) CSIC-Universidad de Zaragoza, Department of Chemical and Environmental Engineering, University of Zaragoza, Campus Río Ebro-Edificio I+D, C/ Mariano Esquillor S/N, 50018, Zaragoza, Spain.

E-mail address: [mbernechea@unizar.es](mailto:mbernechea@unizar.es) (M. Bernechea).

<https://doi.org/10.1016/j.jpowsour.2024.234730>

Received 12 February 2024; Received in revised form 26 April 2024; Accepted 13 May 2024

Available online 18 May 2024

0378-7753/© 2024 The Authors. Published by Elsevier B.V. This is an open access article under the CC BY-NC license (<http://creativecommons.org/licenses/by-nc/4.0/>).

interfaces (SEI) leading to and faster sodium diffusion in the plateau region. Additionally, MPA and EDT treatments have been applied to a soft carbon (Vulcan XC-72R) resulting in a substantial 30 % capacity improvement after 100 cycles at 1C.

These results demonstrate the wide applicability of the method as a straightforward and efficient strategy for improving the electrochemical properties of carbon anodes used in SIBs.

## 1. Introduction

The pursuit of clean energy generation and efficient energy storage systems has become imperative in our society. As the global demand for energy continues to rise, there is a growing need to transition from fossil fuel-based power sources to cleaner alternatives. Therefore, renewable energy sources integration has become the focus of many countries and organizations as they have the potential to reduce greenhouse emissions and fossil fuel dependency. However, one of the primary challenges of renewable energy lies in its storage capabilities. Unlike fossil fuels, that can provide instant energy when required, renewable sources are reliant on climate conditions, resulting in occasional energy peaks and fluctuations in energy generation, including both oversupplies and undersupplies [1]. To address these challenges the development of efficient energy storage systems has become critical. Nowadays lithium-ion batteries (LIBs) are the most used systems in portable electronics and are considered a highly important storage system for short and intermittent energy storage due to their high energy density and design flexibility. Nevertheless, despite their widespread use, they have well-known drawbacks. These limitations include scarcity and limited geographic distribution of key materials like lithium or cobalt, safety issues, and the formation of dendrites [2–4]. In recent years sodium-ion batteries (SIBs) gain a significant interest due to the abundance of sodium, the potential cost-effectiveness, and environmental acceptance. However, one of the major challenges is the development of an anode material able to effectively store sodium ions. While graphite is commonly used as the anode material in standard rechargeable LIBs, it is inadequate for SIBs, due to its inability to form binary compounds with sodium ions [5]. As a result, the identification and development of alternative anode materials for SIBs has become a priority in the field of electrochemical storage research.

In this context, amorphous carbons such as hard carbons (HCs) and soft carbons (SCs), have risen as the most common option for anodes in SIBs. Their low-cost, and environmentally friendly synthesis combined with great storage capacity have placed them in the spotlight in recent years. HCs are currently the preferred anode in commercial SIBs (for example, CATL, Tiamat, and Faradion batteries); however, SIBs using SCs anode are also being commercialized (HiNA Battery) [6]. HCs are mainly obtained from the carbonization of biomass-based precursors. They exhibit great capacity values that can reach 300 mAh·g<sup>-1</sup>, mainly due to their low-potential plateau below 0.1 V vs. Na/Na<sup>+</sup> [7–10]. However, this also results in poor rate performance and low stability [11,12]. In contrast to HCs, SCs are obtained from high-temperature pyrolysis of aromatic compounds. They exhibit a sloping region during both the sodiation and desodiation processes, lacking a low-potential plateau, which results in enhanced stability and better high-rate performance. However, their average capacities tend to be lower than those of hard carbons oscillating between 100 and 250 mAh·g<sup>-1</sup> [9,11,12]. The differences in their sodium storage mechanisms arise from their nanometric structure, where SCs exhibit less curvature and a higher degree of order in the stacking of their graphene layers [12].

One of the most important concepts in the anode performance is the solid electrolyte interphase (SEI) which is crucial for the electrochemistry of sodium ion batteries (SIBs) anodes due to its influence on sodium transport and stability. The term SEI was first introduced in 1979 by Peled when he observed a layer formation on alkali metal upon contact with organic electrolytes [13]. This layer was found to be ionically conductive but nonconductive electronically. In 1997, Peled et al. proposed the “mosaic model” as the prevailing structure, which continues

to be widely accepted in present times [14]. This structure comprises small domains of inorganic, organic salts and polymers which allow the transfer of the ions (Li, Na, K ...) and protects the surface of the anode [15]. These species are formed upon decomposition of the organic electrolyte on the anode surface during the first cycle. This process is influenced by the nature of the organic solvents, electrolyte salt, additives, and functional groups on the anode surface [15,16]. Unfortunately, hard carbons and soft carbons usually form inhomogeneous SEI layers with commercial electrolytes which lead to low initial Coulombic efficiency (iCE), low cycling stability, and poor rate capability [17]. SEI engineering and interface chemistry regulation have risen as possible solutions to improve the LIBs and SIBs performance [18,19]. Different approaches have been proposed to tune the SEI such as: different electrolyte solvents [20,21], electrolyte additives [16,22], oxygen plasma functionalization [23], and atomic layer deposition (ALD) [24]. Another common approach is the coating of HC anodes with SC or preparing HC-SC composites to block open pores, reduce surface area and therefore, decrease the SEI decomposition to enhance the iCE [25,26]. Special attention has been placed on introducing oxygen functional groups on the surface of the carbon anode via chemical oxidation [27] or *in-situ* polymerization of carbonyl-rich molecules to improve wettability and act as active sites for electrolyte decomposition [17]. Additionally, carbon functionalization using molecules has also been explored. Romero-Cano et al. [28] proposed the incorporation of N-rich molecules (urea and melamine) to homogenize the surface chemistry of hard carbons, preventing irreversibility and providing extra capacity storage mechanisms. Yu et al. [29] modified the surface of an HC using 2, 2-dimethylvinyl boric acid (DEBA) to construct a more stable SEI achieving an iCE of 77 % and 90 % capacity retention after 2000 cycles in comparison to the 65 % iCE and 54 % capacity retention of unmodified hard carbon. These surface treatments have shown to improve the capacity, stability, and iCE of pristine carbons; however, most of them require complex techniques, high temperatures, long treatment times, or modifying the synthesis and pyrolysis steps of the carbon.

Two of the most used solvents in SIBs are ethylene carbonate (EC) and dimethyl carbonate (DMC) due to their high dielectric constant, low viscosity, and high ionic mobility. They undergo decomposition upon contact with the anode during the initial sodiation and desodiation cycles mainly forming Na<sub>2</sub>CO<sub>3</sub>, Na<sub>2</sub>O and several polycarbonates [20]. Additionally, additives such as fluoroethylene carbonate (FEC) and the NaPF<sub>6</sub> salt decompose to form NaF [16,30,31]. It has been reported that a high amount of carbonates in the SEI is detrimental to SIB performance [32,33]. On the other hand, other inorganic components of SEI such as Na<sub>2</sub>O and NaF possess higher Na<sup>+</sup> conductivity and migration than organic compounds, which induces better rate capability [17,32], provides high mechanical strength [34], and suppresses the growth of Na dendrites leading to better stability [35–37].

In this work we propose a simple, fast, and low-cost surface treatment at room temperature using short-chain organic molecules: 3-mercaptopropionic acid (MPA), 1,2-ethanedithiol (EDT) and oxalic acid (OxA). They are short-chain ligands of similar size containing functional groups such as thiols (MPA and EDT) and carboxylic acids (MPA and OxA), which can enhance the interaction between the electrode surface and electrolyte, and modify the composition of the SEI [38]. In a previous study, we observed a notable enhancement in the wettability, capacity, and stability of an aqueous supercapacitor electrode upon the introduction of the short-chain organic molecule MPA [39]. However, a deeper study on the reasons behind these improvements was not performed. In this study, we have studied the effect of having different

functional groups on SEI formation, with special emphasis on the formation of carbonates ( $\text{CO}_3^{2-}$ ),  $\text{Na}_2\text{O}$  and NaF contents and their influence on electrochemistry. A corncob-derived carbon (C1400) has been chosen as a hard carbon (HC) model. This hard carbon has proven to be very promising for Na-ion battery anodes, but it exhibited problems with ion blockage related to SEI formation [40]. Given the positive impact of the surface treatments on the hard carbon performance, the best performing treatments have been applied to Vulcan XC-72R (chosen as the soft carbon model), showing a more noticeable capacity improvement. These results demonstrate the versatility and wide applicability of the method for both HCs and SCs.

## 2. Experimental (materials and methods)

### 2.1. Materials

Organic ligands 3-mercaptopropionic acid (MPA), 1,2-ethanedithiol (EDT), and oxalic acid (OxA) were purchased from Sigma Aldrich. Toluene (>98 %), and pure acetonitrile were purchased from VWR Chemicals.  $\text{H}_2\text{SO}_4$  (>98 %) was acquired from ACRO Organics.

Polyvinylidene fluoride (PVDF) ( $M_w \sim 534,000$  (GPC)), sodium chunks, ethylene carbonate (EC), and dimethyl carbonate (DMC) were purchased from Sigma Aldrich. Sodium hexafluorophosphate ( $\text{NaPF}_6$ ), and fluoroethylene carbonate (FEC) were purchased from Alfa Aesar. Super C65 conductive carbon was purchased from Imerys, N-methyl-2-pyrrolidone (NMP) was obtained from Merck, Carbon-coated aluminum foil was acquired from Armor, France, and Vulcan XC-72R was kindly provided by CABOT corporation.

Corncob was obtained from a local field. Preceding the pyrolysis process, the corncob underwent an overnight drying procedure in a dryer maintained at 80 °C. The initial heat treatment was performed within a quartz tube furnace, exposed to a flow of argon ( $15 \text{ L h}^{-1}$ ), during which the temperature was elevated to 900 °C at a rate of  $2.5 \text{ }^\circ\text{C}\cdot\text{min}^{-1}$ . Upon reaching 900 °C, the temperature was sustained for a duration of 1 h before gradual cooling to room temperature. Subsequently, the second phase entailed elevating temperature to 1400 °C using an  $\text{Al}_2\text{O}_3$  tube furnace, while maintaining an argon flow ( $50 \text{ L h}^{-1}$ ). The heating rate was fixed at  $2.5 \text{ }^\circ\text{C}\cdot\text{min}^{-1}$ , and the temperature was held constant for 1 h, followed by cooling to room temperature. After the pyrolysis, the obtained corncob C1400 hard carbon was grinded [40].

### 2.2. Surface treatments

Organic ligand solutions (MPA 1 M, EDT 1 M, and OxA 0.1 M) were prepared by dissolving MPA, EDT, or OxA in acetonitrile or in an acidic acetonitrile solution (0.1 M  $\text{H}_2\text{SO}_4$  in acetonitrile). Two sets of surface-treated samples were prepared with sulfuric acid (CA-L) and without (C-L) to analyze the effect of including the acid. Corncob 1400 °C powder was thoroughly mixed with freshly prepared organic ligand solutions (1 mL of solution per 100 mg of carbon) for 30 min under vigorous stirring. Afterward, samples were washed several times with acetonitrile and toluene and dried at 80 °C overnight. Samples were labeled as C1400 for the original hard carbon material, and C-MPA, C-EDT, and C-OxA for the surface treated samples without  $\text{H}_2\text{SO}_4$ . On the other hand, C1400 carbon treated with sulfuric acid was labeled as CA, CA-MPA, CA-EDT, and CA-OxA when  $\text{H}_2\text{SO}_4$  was included in the ligand solution.

In the case of the soft carbon (Vulcan XC-72R) treatments, the treatment was slightly modified due to the higher porosity of the soft carbon. We added 2 mL of 0.5 M MPA or EDT solutions in acetonitrile per 100 mg of carbon. Samples were labeled as V-MPA or V-EDT.

### 2.3. Electrode preparation and cell assembly

Electrode slurries were prepared with a composition of 90 %wt. of active material (C1400, C-L, CA-L, Vulcan or V-L), 5 %wt. of PVDF

binder, and a 5 %wt. of conductive carbon C65. NMP was used as a solvent. The mixture was ball milled at 300 rpm for 30 min to obtain a homogeneous slurry. The slurry was coated on Al/C foil using a doctor blade applicator resulting in a uniform coating with a thickness of 100  $\mu\text{m}$ . The final coated material underwent an overnight drying process at 80 °C. Subsequently, electrodes with a diameter of 15 mm were cut and stored within an argon-filled glovebox, featuring mass loadings ranging between 1.5 and 2  $\text{mg cm}^{-2}$ .

Two-electrode CR2032 type coin cells were assembled in an argon-filled glovebox with water and oxygen contents below 0.5 ppm. C1400, Vulcan, surface-treated C1400 or surface-treated Vulcan materials were used as working electrodes while sodium metal was used as the counter/reference electrode. Both electrodes were separated by a glass fiber separator. The electrolyte used was 1 M  $\text{NaPF}_6$  dissolved in EC:DMC (1:1 %vol.) with 2 %wt. FEC additive. Each cell was carefully loaded with 100  $\mu\text{L}$  of the electrolyte solution.

### 2.4. Physical characterization

$\text{N}_2$  adsorption measurements were performed using ASAP 2020 gas sorption analyzer from Micromeritics. The degassing step was performed at 120 °C. MicroActive software was used to process the data and obtain the Brunauer-Emmett-Teller (BET) surface area by using Rouquerol procedure. Carbon slit pores by NLDFT model was used for the pore size distribution calculations.

Scanning electron microscopy (SEM) images and Energy-dispersive X-ray spectroscopy (EDX) analysis were performed in a SEM Inspect 50 instrument. Transmission electron microscopy (TEM) images were acquired using a Tecnai F30 microscope operating at 300 kV. Samples were prepared by sonicating carbon powders in ethanol and adding a couple of drops on holey-carbon copper grids. Thermogravimetric analysis (TGA) was performed under  $50 \text{ mL min}^{-1}$   $\text{N}_2$  flow, from 35 °C to 1000 °C at a heating rate of  $10 \text{ }^\circ\text{C}\cdot\text{min}^{-1}$  on a TGA Q5000 IR from TA Instruments. Powder X-ray diffraction (XRD) was performed in an X-ray diffractometer PANalytical Empyrean instrument in Bragg-Brentano configuration using  $\text{Cu K}\alpha$  radiation and equipped with a PIXcel1D detector. Attenuated total reflection Fourier transform infrared (ATR-FTIR) spectra were obtained using a Bruker Vertex-70 FTIR spectrophotometer with a Golden Gate diamond ATR module. Data points were collected from  $3500 \text{ cm}^{-1}$  to  $1000 \text{ cm}^{-1}$  at a resolution of  $4 \text{ cm}^{-1}$  and 512 number of scans. X-ray photoelectron spectroscopy (XPS) of carbon materials was performed with an Axis Supra spectrometer (Kratos Tech). *Ex-situ* X-ray photoelectron spectroscopy (XPS) of cycled electrodes was performed using the Versa probe 3 AD (Physical Electronics, Chanhassen, U.S.A) with a monochromatic  $\text{Al K}\alpha$  X-ray source operating at 15 kV and 13.3 mA. Samples were subjected to cycling at a C/10 rate, comprising one discharge and one charge cycle. Subsequently, the half-cell was disassembled, and the HC electrode was meticulously cleaned using DMC prior to the analysis. Cycled electrodes were put on a non-conductive double-sided scotch tape in the “floating” setup and placed in the center of the XPS holder inside an argon filled glove box. The samples were transferred inside into the XPS intro chamber with a transfer vessel without air exposure. For each sample, spectra were acquired by scanning a  $1 \times 1 \text{ mm}^2$  area with the spot size of 200  $\mu\text{m}$ . Narrow spectra were acquired at a pass energy of 27 eV and step of 0.05 eV to obtain high quality data. Analysis of the peaks was performed with the CasaXPS software using a weighted sum of Lorentzian and Gaussian component curves after Shirley background subtraction. The binding energies were referenced to the internal C1s standard at 284.6 eV.

### 2.5. Electrochemical characterization

The electrochemical characterization was performed by using Maccor Series 4200 or GAMRY equipment. Measurements consisted of charge-discharge C/10 galvanostatic cycling (100 cycles at  $0.03 \text{ A g}^{-1}$ ) or modified galvanostatic cycling (first 5 cycles at C/10 followed by 100

cycles at 1C or 0.3 A g<sup>-1</sup>. Cycling was performed in the voltage range between 2 V and 5 mV. Voltage hold was applied at the lower cut-off for 5 h or until the current dropped to C/100. The theoretical capacity was chosen following the model proposed by *Bommier et al.* [41].

Modified Galvanostatic Intermittent Titration Technique (GITT) measurements were performed at C/10 applied current during 30 min with 2 h of relaxation between steps. Apparent diffusion coefficients were calculated from Fick's second law and linear correlation assumptions [42]. C-rate performance measurements were conducted within a voltage window from 2 V to 0.005 V vs. Na/Na<sup>+</sup>. The protocol included an initial stabilization cycle to form the SEI and 5 consecutive cycles with the current 30 mA h g<sup>-1</sup> (C/10) with applied constant voltage at the lower cut-off until the current drops below C/100 or during a maximum of 5 h. Subsequently, 5 cycles at each respective current were performed. The time limits of the voltage hold were accordingly adjusted to the different C-rates (2.5 h for C/5, 1 h for C/2 ...). Electrochemical Impedance Spectroscopy (EIS) were performed using a 2-electrode half-cell experimental configuration, using an amplitude of 10 mV across a frequency range from 100 kHz to 0.01 Hz. Circuit modeling and data processing was performed using the GAMRY Echem Analyst software.

### 3. Results and discussion

#### 3.1. Physico-chemical characterization of surface-treated materials

Surface-treated materials were prepared by simply mixing the carbon powder with the ligand solution under constant stirring at room temperature for 30 min. At the beginning, sulfuric acid was used for the preparation of the ligand solutions to enhance the bonding between ligands and hard carbon due to its catalytic properties, especially in reactions such as carboxylic acid esterification (Fisher esterification) [43]. But, it was observed that ligands were present on the surface even without acid treatment.

XRD patterns show that surface treatments do not modify the C1400

crystalline structure (Fig. 1a and b). The expected (002) and (100) carbon peaks are distinguished in all materials [40]. With regards to sulfuric acid pretreated samples, the emergence of new peaks was observed, which may be indicative of the formation of sulfate salts (Fig. 1a). This hypothesis was further supported by the disappearance of the peaks after washing the samples with water (Fig. S1). Moreover, C-OxA and CA-OxA show two common peaks at 26° and 30° which might correspond to solid oxalic acid [44]. All samples treated with carboxylic-ending molecules (OxA and MPA) show a new signal at 1680 cm<sup>-1</sup> in the ATR-FTIR spectra (Fig. S2), that is attributed to the C=O stretching vibration of the carboxylic groups. The sample C-OxA shows the signal at 1705 cm<sup>-1</sup> (Fig. S2b) which corresponds to the second harmonic stretching of the same bond [45]. As expected, C1400, CA, CA-EDT or C-EDT samples show no signal at this wavenumber. No S-H stretching signal between 2600 and 2500 cm<sup>-1</sup> has been found for any of the samples probably due to the interaction of sulfur with carbon or deprotonation of the thiol group.

TGA measurements have been performed to quantify and confirm the incorporation of the organic ligands on the carbon surface. Experiments were conducted in a nitrogen atmosphere to identify organic molecules adhered to the carbon surface and to differentiate variations in the strength of chemical bonding as a function of degradation temperature. Mass losses before 150 °C are attributed to adsorbed solvents and water [46]. Samples treated in acidic media are compared with sulfuric acid-treated carbon (CA) in Fig. 1c, and the surface treated samples are compared with the native carbon (C1400) in Fig. 1d. Mass losses in CA are attributed to the decomposition of surface functional groups and degradation of C-SO<sub>x</sub> generated by interaction with the acid (240 °C–350 °C) [47]. As expected, additional degradations are observed at 190 °C for CA-OxA, 230 °C for CA-EDT, and 200–235 °C for CA-MPA, attributed to molecules chemically bonded to the carbon through C-O and C-S bonds [46–49]. The difference in degradation temperature suggests that MPA and EDT are more strongly bound to the carbon than OxA. Moreover, CA-MPA and CA-EDT samples show an additional mass loss at 350 °C, which can indicate C-S interaction between thiols and

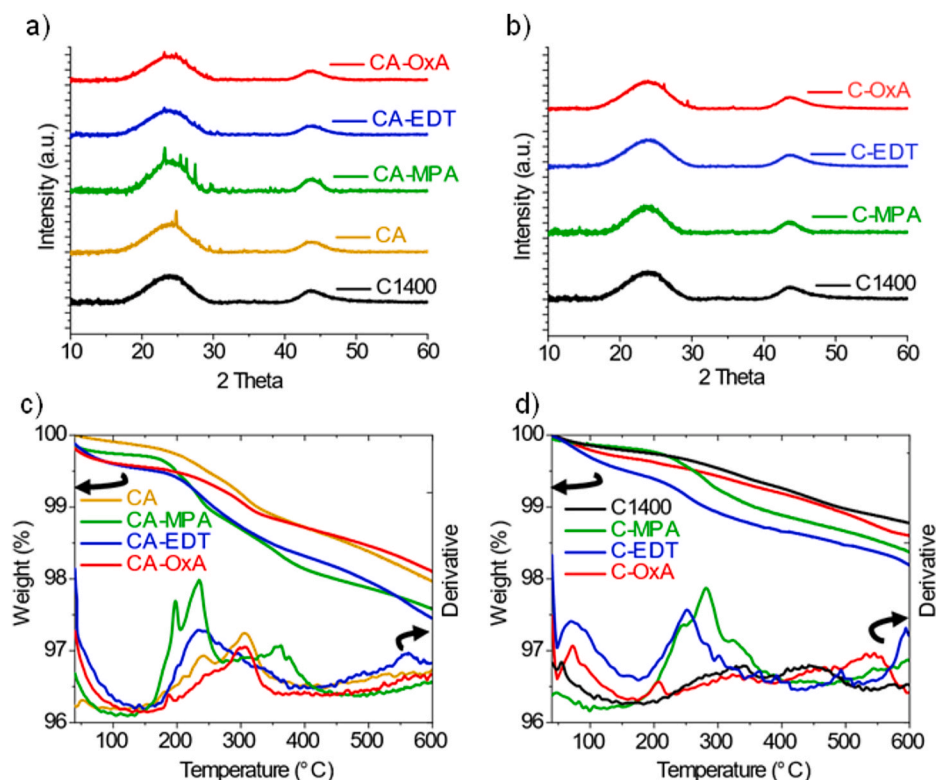


Fig. 1. XRD patterns of C1400, (a) CA-L samples and (b) C-L samples. TGA curves of the (c) CA-L and (d) C-L; both under N<sub>2</sub> atmosphere.

carbon surface, or aliphatic carbons bonded to oxygen ( $C_{al-O}$ ) [47]. Non pretreated carbon (C1400, Fig. 1d) shows two mass losses at 330 °C and 450 °C due to the decomposition of functional surface groups. Besides, surface-treated materials show their first degradation at 205 °C for C-OxA, 250 °C for C-EDT and 282 °C for C-MPA with a shoulder at 230 °C. Again, MPA and EDT appear to be more strongly bonded to carbon than OxA. These results evidence the successful functionalization of the carbon with the three ligand molecules regardless of the presence of sulfuric acid in the treatment. Furthermore, loadings of the different ligands have been compiled in Table 1. MPA and EDT loading is around 0.5 %wt. and 0.2 %wt. for OxA. The utilization of sulfuric acid seems to have a negligible impact on the quantity of incorporated ligands.

TEM and SEM imaging shows that surface treatments have no visible impact on the topology of the carbon surface (Fig. S3). SEM-EDX semi quantitative analysis (Table S1) shows that all C1400 samples pretreated with sulfuric acid show at least 0.5 %wt. S content attributed to the presence of sulfates (further confirmed in the XPS analysis, Fig. 2c). Moreover, C-MPA and C-EDT samples have around 0.5 %wt. S content attributed to the presence of MPA and EDT molecules. No sulfur is detected for C1400 or C-OxA. No significant differences in ligand loading are observed in the presence of sulfuric acid. Despite several washings, K and Si from lignocellulose precursors are still detected in the analysis [40].

XPS analyses have been performed to corroborate the incorporation of the ligand molecules onto the carbon surface. Elemental quantification is summarized in Table 2. C 1s, O 1s and S 2p are the main narrow spectra that have been studied for this purpose.

The C 1s peak fitting (Fig. 2a and b) shows the same three components for all the materials, corresponding to C-C/C=C, C-O/C-S and C=O from lower to higher binding energy (BE). For molecules with carboxylic acid groups (CA-MPA, CA-OxA, C-MPA, and C-OxA) an additional peak at around 289 eV, assigned to the presence of -COOH, has been observed. This signal is not detectable in the other samples. The peak fitting of O 1s spectra follows the same tendency (Fig. S4).

All materials show C=O, C-OH/C-O-C signals and CA-MPA, CA-OxA, C-MPA, and C-OxA have an additional component at higher BE assigned to -COOH [50,51]. Both, C 1s and O 1s, confirm the successful incorporation of OxA and MPA on the carbon surface. Besides, S 2p narrow spectra were studied to confirm the presence of sulfur species in MPA and EDT samples (Fig. 2c). The presence of sulfates has been detected in all samples, with a comparatively higher concentration observed in samples pretreated with sulfuric acid. Moreover, C-MPA, CA-MPA, C-EDT, and CA-EDT display a characteristic  $2p_{3/2}$  signal at approximately 163.3 eV, which can be attributed to the presence of C-S-C bonds [52,53] thereby verifying the bonding between carbon and molecule thiol groups. Oppositely, as expected, C1400, CA, C-OxA, and CA-OxA do not exhibit such signals. In both cases, CA-L and C-L covalent

bonding between carbon and molecule is detected regardless of the incorporation of sulfuric acid in the functionalization. These findings are consistent with the conclusions drawn from the TGA curves.

### 3.2. Electrochemical characterization

CA-L, C-L and pristine C1400 were used to fabricate electrodes for their testing in half-cell Na-ion batteries. Initially, CA-L samples were subjected to galvanostatic cycling at C/10, during 100 cycles (Fig. 3a and Table 3). A slight increase in capacity is observed for the surface-treated samples, with an 8 % capacity improvement for CA-MPA in the 100th cycle and a 6 % for CA-EDT and CA-OxA. It is noteworthy that the CA sample (C1400 pretreated only with sulfuric acid) shows a 2 % capacity improvement, which makes it very similar to C1400; however, it degrades faster than the other samples. Comparing the capacity in the 2nd cycle and 100th cycle, CA shows capacity retention of 84 %, lower than the 91 % observed for C1400 and CA-OxA, and 87 % for CA-EDT and CA-MPA. Additionally, all samples exhibit Coulombic efficiencies values close to 100 % during the 100 cycles (Fig. S5). Furthermore, surface-treated samples show improved iCE than C1400, that indicates the decrease of charge required for the formation of the solid electrolyte interphase (SEI) (Table 3). Additionally, to get a better insight into the effects of the ligands, samples without acid, C-L, were cycled under the same conditions at C/10 (Fig. 3d). C-MPA and C-EDT are the best treatments exhibiting 12 % and 6 % capacity improvement at 100th cycle respectively in comparison to pristine C1400. C-OxA shows a worse performance and stability. In terms of capacity, there are no differences between C-MPA, C-EDT and their acid counterparts but C-MPA and C-EDT show slightly better stability (93 % and 89 % capacity retention from the 2nd up to 100th cycle) (Table 3). Furthermore, iCE is increased for the three treatments and Coulombic efficiencies are stable and close to 100 % during the 100 cycles of C-MPA and C-EDT (Fig. S5). In summary, most surface treatments have a positive effect on the electrochemical performance of C1400. Notably, MPA and EDT exhibit better performance, regardless of the presence or absence of acid. Additionally, the stability of the materials is enhanced.

Additionally, galvanostatic cycling at 1C was also performed to identify the influence of the treatments at higher C-rates (Fig. S6) where hard carbons might show more limitations. The C1400 reference sample exhibits a decline in capacity after 55 cycles, most likely due to FEC consumption, whereas the surface-treated samples demonstrate enhanced stability, improved capacity and a delayed FEC consumption. Among them, C-L appears to be the most promising materials, with a notable emphasis on C-MPA and C-EDT with capacity improvements in the 100th cycle up to 13 % for C-MPA and 18 % for C-EDT and a capacity retention of 93 % for C-MPA and 95 % for C-EDT vs. 83 % for C1400 at higher C-rates (calculated from cycle 6 to 100).

Capacity, stability, and iCE enhancements are hypothesized to stem from differences in SEI formation and composition. This process is contingent upon the interactions between the surface groups of the carbon material and the electrolyte. The first Na charge-discharge curve is useful to see different SEI formation and to calculate iCE (Fig. 3b for CA-L and Fig. 3e for C-L samples). These curves represent the first discharge (sodiation)-charge (desodiation) cycle at C/10, between 2 V and 0 V vs. Na/Na<sup>+</sup>. A typical curve shows a sloping region (attributed to the adsorption of Na<sup>+</sup> ions onto defects of the material) from high potentials up to 0.1 V and a plateau region below 0.1 V, attributed to the intercalation of Na<sup>+</sup> ions between carbon layers and pore filling by Na atoms. It is observed that in all samples the capacity improvement comes from both the sloping (above 0.1 V) and plateau (below 0.1 V) regions. To gain further insight, a detailed analysis of the inverse derivatives ( $(dV/dx)^{-1}$ ) of this 1st cycle was conducted (Fig. 3c for CA-L samples and Fig. 3f for C-L samples). Two peaks can be distinguished corresponding to the SEI formation reactions [54]. In all samples, the first peak appears in discharge at around 1.1 V vs. Na/Na<sup>+</sup> and it is attributed to the decomposition of the FEC additive. To confirm this, the first cycle

**Table 1**

TGA quantification of surface treated samples. Mass losses within the range of chemical bonding (150 °C–300 °C), C-S bonds or  $C_{al-O}$  (300 °C–400 °C) and stronger interactions (400 °C–600 °C) have been considered. Quantification of ligands was calculated from the difference between the total mass loss of the treated material and their respective reference material, C1400 or CA.

Material	Mass loss (%)	Mass loss (%)	Mass loss (%)	Ligand (% wt.)
	150 °C–300 °C	300 °C–400 °C	400 °C–600 °C	
CA	0.5	0.5	0.7	–
CA-MPA	1.0	0.6	0.5	0.4
CA-EDT	0.8	0.6	0.9	0.6
CA-OxA	0.7	0.6	0.6	0.2
C1400	0.3	0.2	0.5	–
C-MPA	0.6	0.4	0.5	0.5
C-EDT	0.6	0.3	0.5	0.4
C-OxA	0.4	0.2	0.6	0.2

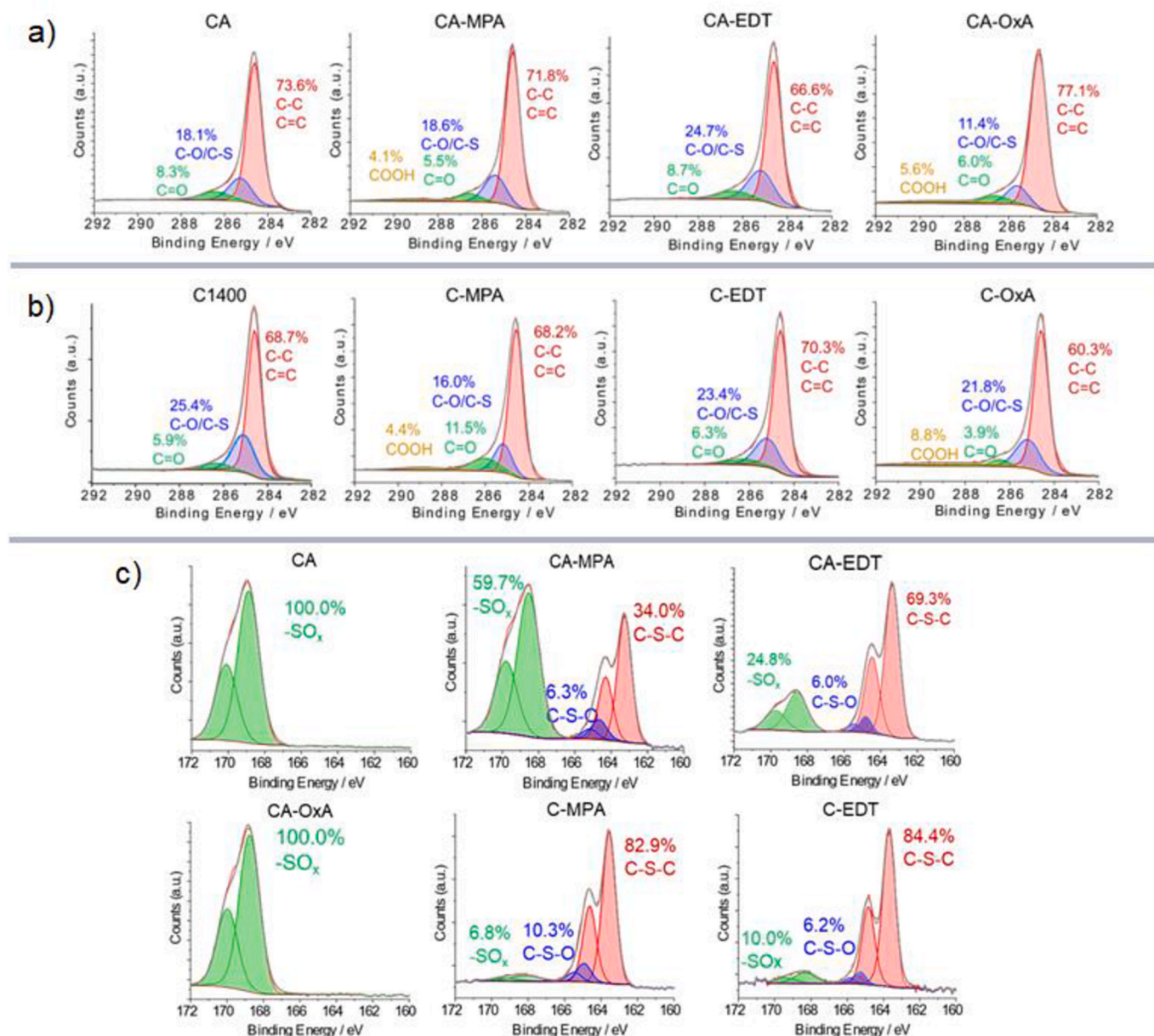


Fig. 2. XPS peak fitting of (a) C 1s spectra of CA-L materials, (b) C 1s spectra of C1400 and C-L materials, and (c) S 2p spectra of CA, CA-MPA, CA-EDT, CA-OxA, C-MPA, and C-EDT.

**Table 2**  
XPS quantification of C1400 and surface-treated samples.

Material	C (%at.)	O (%at.)	S (%at.)	K (%at.)	Si (%at.)
CA	90.5	7.6	1.0	0.3	0.5
CA-MPA	87.7	9.1	2.8	0.2	0.2
CA-EDT	85.7	8.3	4.8	1.1	0.2
CA-OxA	86.0	9.8	2.0	1.8	0.3
C1400	88.7	7.4	0.0	3.7	0.2
C-MPA	90.8	6.1	2.1	0.6	0.3
C-EDT	88.4	5.5	3.4	2.0	0.7
C-OxA	92.8	5.3	0.0	1.6	0.3

was performed in the same conditions without additive in electrolyte by using the C1400 sample (1 M NaPF<sub>6</sub> in EC:DMC). As can be seen in Fig. S7, the peak at 1.1 V vs. Na/Na<sup>+</sup> is not visible. Significant disparities are not observed in the initial peak among any of the samples, as it primarily depends on the presence of the FEC additive.

Hence, the main focus is put on the second peak, which emerges between 0.6 V and 0.7 V vs. Na/Na<sup>+</sup>. This peak is associated with EC and DMC decomposition and the formation of  $-\text{CO}_3^{2-}$  species (polycarbonates, alkyl carbonates and Na<sub>2</sub>CO<sub>3</sub>) [20,55]. Depending on the treatment applied, the peak appears at different voltage suggesting differences in the decomposition process (Table 3) [56]. More precisely, the peak in CA-MPA and CA-EDT samples is less prominent and shifted to a higher voltage (0.73 V vs. Na/Na<sup>+</sup>) which might suggest that Na<sub>2</sub>CO<sub>3</sub> and polycarbonate formation are less favorable (Fig. 4c) [56, 57]. On the other hand, CA and CA-OxA show lower voltage values (0.66 V and 0.67 V vs. Na/Na<sup>+</sup>). We speculate that  $-\text{CO}_3^{2-}$  formation could be enhanced by the presence of carboxylic groups, as discussed later in *ex-situ* XPS studies. Finally, two great peaks in the 0V–0.1 V vs. Na/Na<sup>+</sup> region are found in the discharge and charge processes, attributed to sodium insertion and de-insertion, respectively (Fig. S8). Non-acid pretreated samples (C-L, Fig. 3f) were examined, and similar correlations were identified. In C-MPA and C-EDT, the peak associated with solvent decomposition appears at higher voltages (0.7 V vs.

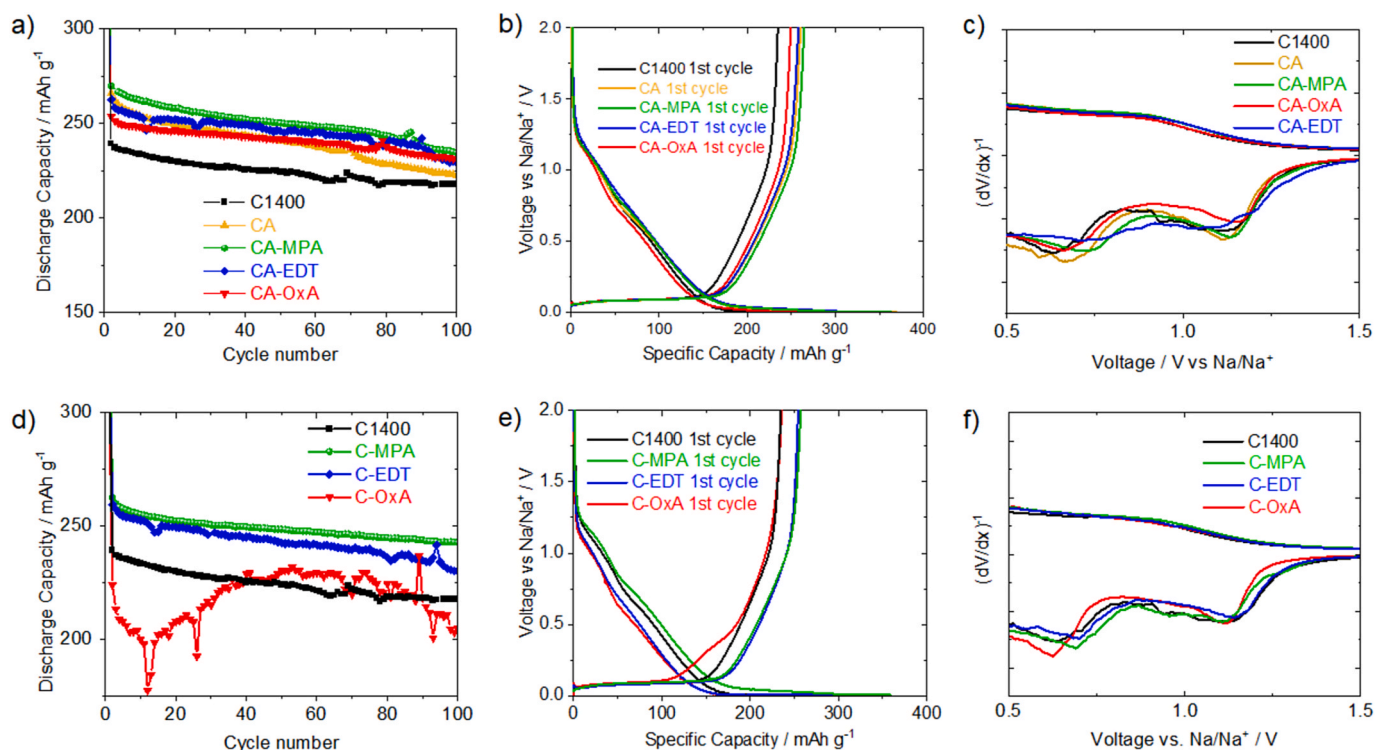


Fig. 3. Galvanostatic cycling at C/10 (a) Capacity vs. cycle number of CA-L samples, (d) Capacity vs. cycle number of C-L samples. Capacity axis have been adjusted to better visualize the capacity and stability effects during cycling. Charge-discharge curve in the first cycle of (b) CA-L and (e) C-L samples. Differential Capacity vs. Voltage first cycle magnification in the 0.5–1.5 V vs. Na/Na<sup>+</sup> region of (c) CA-L and (f) C-L samples.

Table 3

Summary of the electrochemistry features of C1400 and surface treated materials cycled at C/10.

Material	100th cycle (mAh·g <sup>-1</sup> )	Capacity retention (%) <sup>a</sup>	Capacity improvement (%) <sup>b</sup>	iCE (%)	1st peak (V)	2nd peak (V)
CA	223	84	2	71	1.11	0.67
CA-MPA	235	87	8	73	1.14	0.73
CA-EDT	229	87	6	71	1.11	0.73
CA-OxA	231	91	6	74	1.15	0.66
C1400	217	91	–	70	1.13	0.63
C-MPA	243	93	12	72	1.11	0.70
C-EDT	230	89	6	75	1.14	0.70
C-OxA	205	91	–	73	1.11	0.60

<sup>a</sup> Calculated from the 100th relative to the 2nd cycle.

<sup>b</sup> Calculated from the 100th cycle and compared to the C1400.

Na/Na<sup>+</sup>), whereas C-OxA exhibited the peak at 0.6 V vs. Na/Na<sup>+</sup>, thus substantiating the previously drawn conclusions.

Once the electrodes are stabilized, it is possible to differentiate between adsorption, intercalation and pore filling. The 100th charge–discharge curve and adsorption/insertion/pore filling column graphs were compared to clarify which step is most significantly influenced by surface treatments (Fig. S9). At both C-rates (C/10 and 1C) surface treatments seem to enhance both sodium insertion and adsorption. This effect is particularly noticeable in MPA and EDT treatments, especially at the higher rate of 1C, where HCs encounter more challenges.

In summary, adding sulfuric acid to the surface treatment does not seem to provide any benefit regarding the amount of ligand loaded. Furthermore, the electrochemical results closely resemble those of the non-acid counterparts. Consequently, the primary focus of subsequent studies has been directed towards the C-L samples.

To gain deeper insights into the underlying processes and the impact of each ligand on the electrochemical processes, N<sub>2</sub> adsorption and GITT measurements were conducted on C-L samples. Tuning the size or

blocking the micropores entrance is a common strategy to avoid the undesired entry of solvated sodium ions into the pores [58,59]. If solvated ions enter the micropores, they can get trapped because of their large size. Therefore, blocking the pores reduces this loss. Moreover, the increase in the external surface area forces sodium storage through intercalation in the carbon matrix. Alternatively, if the micropore size is reduced, the sodium ions are forced to enter the pores without solvent molecules. Non-solvated ions enter and leave pores more easily leading to reversible storage of Na ions and improved iCE [25,26,60]. Our results suggest that short-chain ligands can partially block the material micropores increasing the carbon external surface area (Table S2). These data align with the improvement in the intercalation and the decrease in pore filling contribution, indicating a consistent trend in the observed results. GITT measurements (Fig. S10) were performed at C/10 with C1400 and C-L samples (Fig. 4) to calculate the apparent sodium diffusion coefficients (D) of the materials using the following formula:

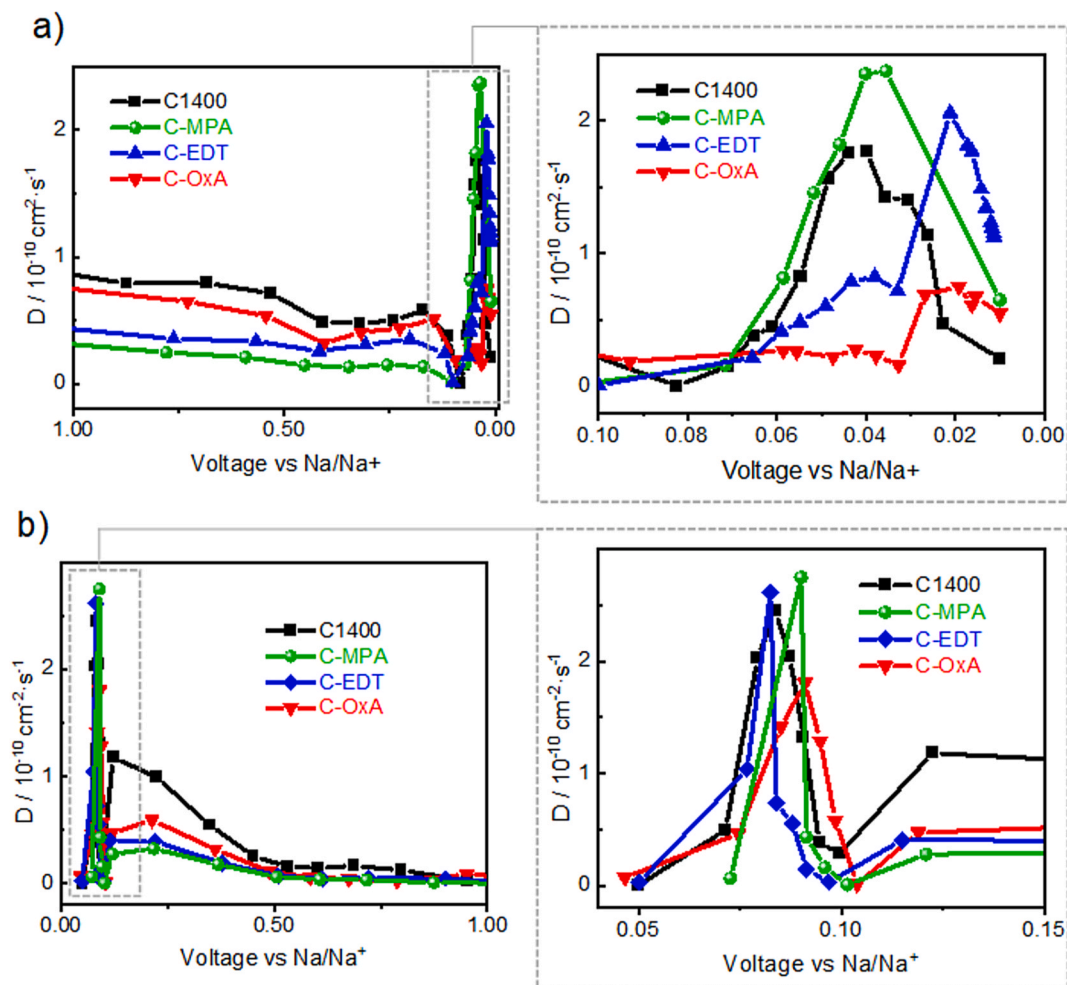


Fig. 4. Na-ion apparent diffusion coefficients calculated from the corresponding C1400 and C-L GITT profiles for (a) discharge and (b) charge with magnified views of the plateau region.

$$D = \frac{4}{\pi\tau} \left( \frac{m_B V_M}{M_B S} \right)^2 \left( \frac{\Delta E_S}{\Delta E_t} \right)^2$$

where  $V_M$  is the molar volume and  $M_B$  is the molar mass; both can be substituted by the inverse of the material density ( $1.973 \text{ g cm}^{-3}$  for C1400 [40], and  $0.096 \text{ g cm}^{-3}$  for Vulcan, according to producer data). Same density values were used for their respective surface treated materials.  $\tau$  is the relaxation time,  $m_B$  is the active mass in the electrode and  $S$  is the electrode area.  $\Delta E_S$  corresponds to the steady-state voltage change and  $\Delta E_t$  to the transient voltage change. The main assumptions are that the electrode material is homogeneous, the molar volume change of the active material during charge or discharge is not large enough and the current should be a low value with a short duration time.

All samples exhibit similar  $D$  values which remain mostly constant during the sloping region. At  $0.1 \text{ V vs. Na/Na}^+$ , an abrupt decrease is observed due to the different mechanism of sodiation at the beginning of the plateau region. Afterward,  $D$  sharply increases displaying the typical U-shape of hard carbons to later decrease again near the cut-off voltage. C-OxA and especially C-MPA and C-EDT show a less pronounced decrease at  $0.1 \text{ V vs. Na/Na}^+$  than C1400, which indicates that these materials would be less susceptible to polarization and display a better rate capability [61,62]. Indeed, C-L samples show better performance at 1C cycling than the untreated carbon (Fig. S6b). Moreover,  $D$  values of C-MPA and C-EDT in the plateau region (below  $0.1 \text{ V vs. Na/Na}^+$ ) and near to the cut-off voltage are higher than C1400 and C-OxA ones. This indicates a faster diffusion of sodium during intercalation in the carbon

matrix in C-MPA and C-EDT [61,62]. Furthermore,  $D$  values for desodiation cycle (Fig. 4b), exhibit similar tendencies. C-MPA and C-EDT have slightly higher  $D$  values in the intercalation region and a smoother transition into the adsorption mechanism at  $0.12 \text{ V vs. Na/Na}^+$ .

Galvanostatic cycling tests at different C-rates for C-L samples was performed (Fig. S11). C-MPA and C-EDT demonstrate enhanced performance as compared to C1400 and C-OxA, with C-EDT showing slightly superior performance at higher C-rates. To better understand the involved processes, electrochemical impedance spectroscopy (EIS) measurements were conducted (Fig. S12, Note S1). C-MPA and C-EDT exhibit significantly lower resistivity (Table S3) in the SEI region ( $85.6\Omega$  and  $58.5\Omega$ ) than C1400 and C-OxA ( $182.7\Omega$  and  $265.7\Omega$ ), indicating a more favorable  $\text{Na}^+$  ion diffusion through the SEI. Moreover, these results point at a superior stability and electrochemical performance after the 40 cycles at different C-rates.

Based on these results, it is clear that carbons treated with molecules containing  $-\text{SH}$  groups exhibit better performance, faster sodium diffusion in the plateau region, and improved micropore blockage [58,59]. It is probable that the presence of  $-\text{COOH}$  groups favors  $\text{CO}_3^{2-}$  formation while  $-\text{SH}$  groups might lead to a more favorable SEI composition that directly affects capacity, stability, and iCE. For this reason, and to confirm the hypothesis, *ex-situ* XPS characterization of the electrodes has been conducted to identify and understand the SEI composition differences and their relationship with the functional groups of the organic ligands.

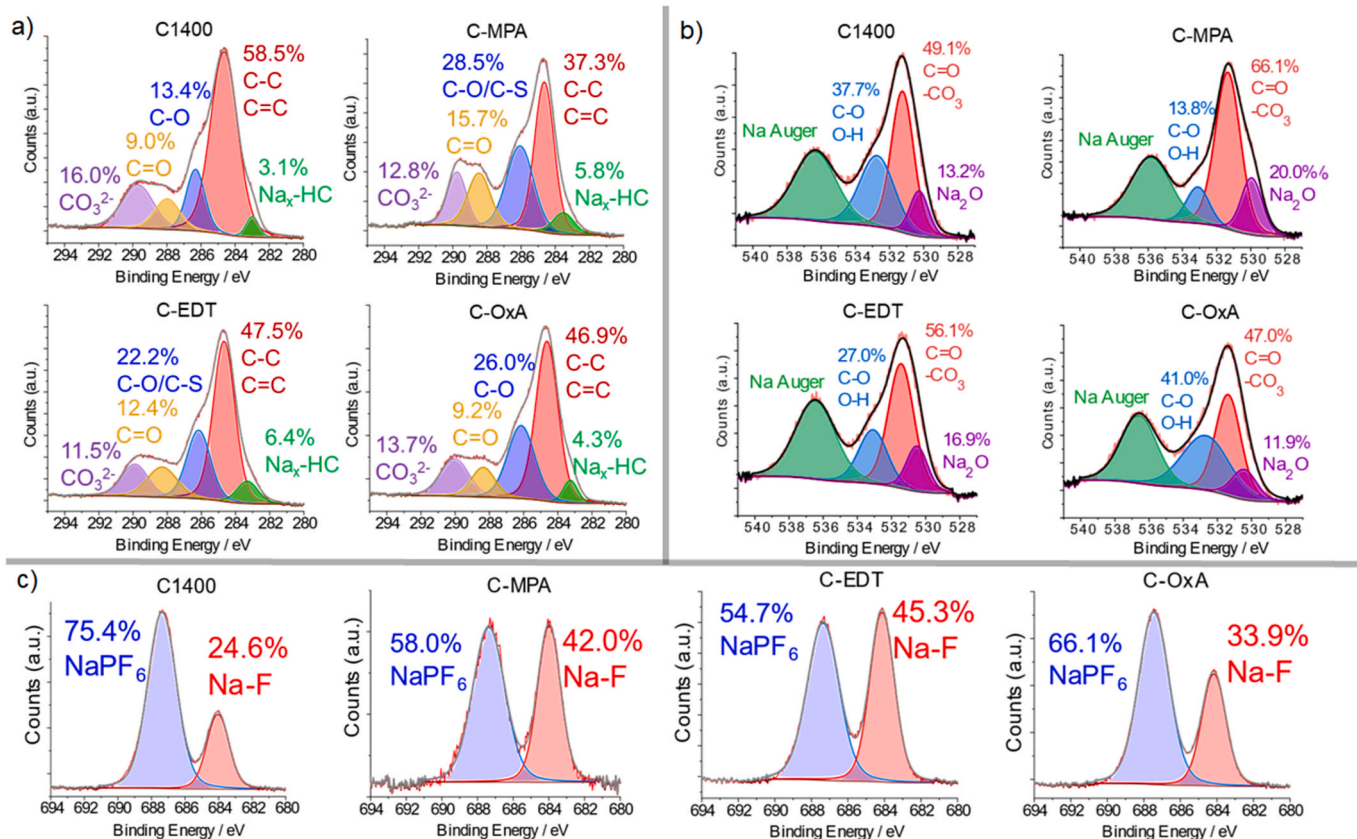


Fig. 5. XPS fitting of (a) C 1s, (b) O 1s, and (c) F 1s *ex-situ* spectra of samples C1400, C-MPA, C-EDT and C-OxA after one charge–discharge cycle at C/10.

### 3.3. Understanding SEI composition – *Ex-situ* XPS

*Ex-situ* XPS analysis after the first discharge–charge cycle enables the determination and quantification of the primary components and species of the SEI formed on the surface of the carbon electrode. In order to monitor NaF,  $-\text{CO}_3^2-$ ,  $\text{Na}_2\text{O}$  and organic species formation, special emphasis has been placed on C 1s, O 1s and F 1s narrow spectra. All analyzed samples have been discharged (sodiated)–charged (desodiated) at C/10 to ensure an adequate formation of the SEI and make them comparable. The discussion focuses on C-L surface-treated samples, but similar results are observed for CA-L samples (Fig. S13). As compared to non-cycled materials (Fig. 2), in the C 1s narrow spectra (Fig. 5a) two additional components at 283 eV and around 290 eV have been detected. The first one at 283 eV corresponds to sodium intercalated into the hard carbon  $\text{Na}_x\text{-HC}$  [33,63]. This signal has been experimentally confirmed in literature through argon etching of the SEI [33], and can be used as an indicator of SEI thickness [63]. Considering that the maximum XPS penetration depth is approx. 10 nm, a more prominent  $\text{Na}_x\text{-HC}$  signal in XPS could be correlated with a thinner SEI [64]. It has been reported that a thinner SEI can improve  $\text{Na}^+$  ion

Table 4

SEI composition summary from *ex-situ* XPS analysis after the first cycle at C/10 for C1400 and C-L samples. Discharge capacities correspond to the 100th cycle of the galvanostatic cycling at C/10.

Material	C 1s		O 1s	F 1s	Dis. Cap. ( $\text{mAh}\cdot\text{g}^{-1}$ )
	$\text{Na}_x\text{-HC}$ (%) at.)	$-\text{CO}_3^2-$ (%) at.)	$\text{Na}_2\text{O}$ (%) at.)	NaF (%) at.)	
C1400	3.1	16.0	13.2	24.6	217
C-MPA	5.8	12.8	20.0	42.0	243
C-EDT	6.4	11.5	16.9	45.3	230
C-OxA	4.3	13.7	11.9	33.9	205

transport [65]. The second signal at 290 eV corresponds to  $-\text{CO}_3^2-$ , attributed to the formation of polycarbonates and  $\text{Na}_2\text{CO}_3$  in the SEI [53, 63]. Furthermore, *ex-situ* O 1s peak fitting reveals several differences compared to the analyses conducted before cycling. The  $-\text{COOH}$  signal (534–535 eV) is not clearly detected; however, two additional components emerge, one at lower energy bindings (531 eV) attributed to  $\text{Na}_2\text{O}$ , and another at higher energy bindings (536 eV), representing the Na Auger signal (Fig. 5b). Besides, F 1s *ex-situ* XPS fitting after the first discharge–charge display two components corresponding to the  $\text{NaPF}_6$  electrolyte (687 eV) and the NaF (684 eV) formed in the SEI (Fig. 5c) [35,53]. For the following *ex-situ* XPS discussion, all the percentages correspond to atomic percentages and as commented, the focus will be on C 1s peak fitting ( $-\text{CO}_3^2-$  and  $\text{Na}_x\text{-HC}$  components), F 1s (NaF component) and O 1s ( $\text{Na}_2\text{O}$ ). Results are summarized in Table 4 and element composition is compiled in Table S4.

Starting with C 1s, C1400 SEI has higher  $-\text{CO}_3^2-$  content (16.0 %at.) than other samples. C-MPA and C-EDT, which have shown the most positive electrochemistry results, seem to have a thinner SEI (5.8 %at. and 6.4 %at.  $\text{Na}_x\text{-HC}$ , respectively) with reduced amounts of  $-\text{CO}_3^2-$  (12.8 %at. and 11.5 %at., correspondingly). On the other hand, C-OxA has similar values to C1400 and exhibits the worst performance. The correlation between the chemical SEI composition and the electrochemical behavior is evident. The presence of short-chain ligands and appropriate functional groups on the carbon surface promotes the formation of a thinner SEI and prevents unnecessary electrolyte decomposition (i.e., showing higher iCE values). This is clearly evidenced in the 1C electrochemistry of C-L and CA-L materials, where the sudden capacity fading attributed to FEC consumption, is notably delayed (Fig. S6). EDT and MPA treatments (both containing  $-\text{SH}$  groups) display a higher  $\text{Na}_x\text{-HC}$  content, which has been reported to be associated with a thinner SEI, and have lower  $-\text{CO}_3^2-$  content, which can result in higher ionic conductivity. On the other hand, the treatment with ligands containing only

–COOH groups (C-OxA samples) promotes the formation of  $-\text{CO}_3^{2-}$  which can hinder the performance.

O 1s detailed spectra have been studied to gain insight into the inorganic compound  $\text{Na}_2\text{O}$  (Fig. 5b). Peak fitting of C-MPA and C-EDT spectra demonstrate higher quantities of  $\text{Na}_2\text{O}$  (20.0 %at. and 16.9 %at., respectively) than C1400 (13.2 %at.) which can result in better stability and improved  $\text{Na}^+$  conductivity. C-OxA components are very similar to C1400 results with lower amount of  $\text{Na}_2\text{O}$  (11.9 %at.) which explains its hindered performance. These results align with the previous C 1s conclusions.

Furthermore, F 1s narrow spectra were analyzed (Fig. 5c). In this context, the NaF component stands out as particularly intriguing, given that a NaF-rich SEI has demonstrated advantageous effects such as better Na diffusion. Carbons treated with ligands: C-MPA (42.0 %at.), C-EDT (45.3 %at.) and C-OxA (33.9 %at.) show an increased amount of NaF content than C1400 (24.6 %at.) which can justify the enhanced electrochemistry of the C-L samples.

In particular, carbons treated with thiol-containing molecules (MPA and EDT) show the highest content of  $\text{Na}_2\text{O}$  and NaF in their SEI, related to better cycling,  $\text{Na}^+$  diffusion, and capacity retention. It is likely that the presence of thiol groups can promote the coordination of  $\text{Na}^+$  on the surface of the electrode leading to an enrichment in sodium species ( $\text{Na}_2\text{O}$  and NaF) during the SEI formation. These results are consistent with the GCD,  $\text{N}_2$  adsorption, GITT, and C 1s *ex-situ* XPS conclusions.

As commented, C 1s, F 1s and O 1s spectra of samples treated in the presence of acid (CA-L) have also been analyzed and the conclusions are similar, with CA-MPA and CA-EDT showing the best results (Fig. S13 and Table S5).

C-MPA and C-EDT treatments exhibited the highest specific capacities with excellent retention after 100 cycles (93 % and 89 %), blocked micropores, higher  $\text{Na}^+$  diffusion in the plateau region and a thinner SEI with increased amounts of  $\text{Na}_2\text{O}$ , NaF and lower amounts of  $-\text{CO}_3^{2-}$ . It can be concluded that thiol-containing ligands without acid are the most beneficial surface treatments for the carbon anode in SIBs.

### 3.4. Ligand treatments to soft carbon

In light of the positive results observed with hard carbon treated with MPA and EDT, we decided exploring whether this surface treatment could enhance the performance of other carbon types used in commercial SIBs, such as soft carbons. For this reason, Vulcan XC-72R carbon black was treated with these molecules (V-MPA and V-EDT) and tested as anodes in SIBs half-cells. ATR-FTIR analysis of Vulcan, V-MPA, and V-EDT (Fig. S14) shows similar trends than observed for hard carbon (HC). The V-MPA spectrum shows a new signal at  $1680\text{ cm}^{-1}$ , attributed to the C=O vibration of the MPA carboxylic group. TGA analysis confirms the successful loading of MPA and EDT. Their curves show important mass losses within the range of chemical bonding ( $150\text{ }^\circ\text{C}$ – $400\text{ }^\circ\text{C}$ ) when compared to pristine Vulcan (Fig. S15). The total amount of ligands is 1

%wt. for both samples. The higher surface area of Vulcan allows for a slightly higher loading of organic molecules than C1400. Capacity improvements have been observed for both treatments during 100 cycles at C/10. As compared to pristine Vulcan XC-72R ( $136\text{ mAh}\cdot\text{g}^{-1}$  at 100th cycle), V-MPA shows an 18 % capacity improvement ( $161\text{ mAh}\cdot\text{g}^{-1}$ ) and V-EDT a 16 % increase ( $158\text{ mAh}\cdot\text{g}^{-1}$ ) (Fig. 6a). At a higher current, 1C, greater improvements are observed at the 100th cycle for both V-MPA and V-EDT. V-MPA showed a 23 % capacity improvement ( $155\text{ mAh}\cdot\text{g}^{-1}$ ) and V-EDT 31 % ( $165\text{ mAh}\cdot\text{g}^{-1}$ ) in comparison to Vulcan ( $126\text{ mAh}\cdot\text{g}^{-1}$ ) (Fig. 6b).

Additionally,  $\text{N}_2$  adsorption shows a similar tendency where micropores are partially blocked with MPA while the external surface is promoted resulting in better and reversible insertion/deinsertion of sodium (Table S6). Apparent diffusion coefficients of Vulcan and V-MPA were also calculated at C/10 (Fig. S16). The shape is consistent with a sloping region attributed to the adsorption of sodium on the surface, and the absence of U-shape, compatible with the reduced intercalation observed in soft carbons [66]. During the whole discharge (sodiation) process, V-MPA shows higher diffusion values, while they are similar for both materials (V-MPA and Vulcan) during charge (desodiation).

## 4. Conclusions

Surface treatments using various short-chain organic ligands (MPA, EDT OxA), both with and without acid, have been applied to hard carbon material and has been tested as anode in SIBs. The treatments have been beneficial for the electrode material showing excellent stability after 100 cycles and an improvement in capacity up to 12 % at C/10 and 18 % at 1C. Additionally, iCE is increased to 14 % in the best cases in comparison to the pristine material. Treatments with ligands incorporating thiol groups (C-MPA and C-EDT) have proven to be the most advantageous. The reasons behind these improvements have been studied using *ex-situ* XPS,  $\text{N}_2$  adsorption, and GITT. Best performing materials show a thinner SEI with lower  $-\text{CO}_3^{2-}$  amount and higher NaF and  $\text{Na}_2\text{O}$  content related to better Na diffusion, as confirmed by GITT measurements in the plateau region.  $\text{N}_2$  adsorption measurements have shown micropore blocking and an increase of external surface area which seems to favor sodium insertion and extraction.

Moreover, MPA and EDT treatments have also been applied to soft carbon Vulcan XC-72R and tested as the anode in SIBs half-cells. Capacity enhancement has been observed especially at higher charge–discharge rates (1C) showing more than a 30 % capacity improvement with great stability after 100 cycles. Again, micropore blocking and increased  $\text{Na}^+$  diffusion seem to be responsible for this enhancement.

In summary, we have shown that a simple, fast, low temperature treatment with short-chain organic ligands can improve the performance of carbon materials used as anodes in SIBs. Moreover, these treated-carbons show good performance at fast charge–discharge rates,

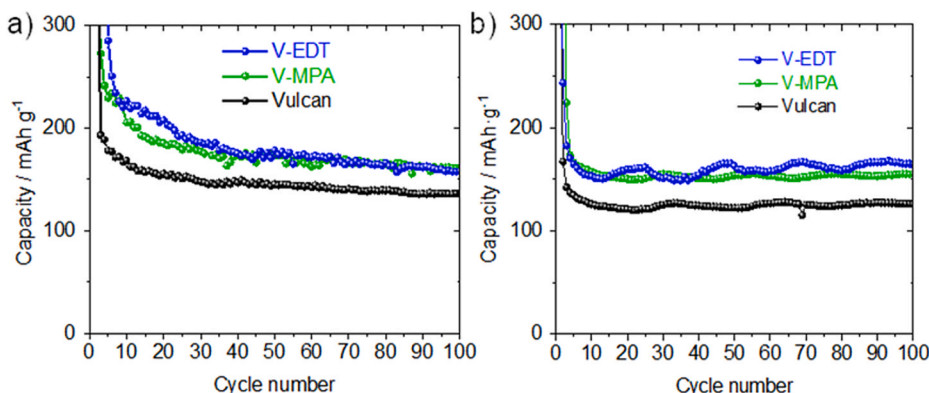


Fig. 6. Galvanostatic cycling capacity vs. cycle number at of Vulcan, V-MPA and V-EDT at (a) C/10 and (b) 1C.

which could be especially relevant for certain applications such as electric mobility.

### CRediT authorship contribution statement

**Sergio Aina:** Writing – original draft, Investigation, Formal analysis, Data curation. **Blaz Tratnik:** Writing – review & editing, Investigation, Data curation. **Alen Vizintin:** Writing – review & editing, Supervision, Investigation, Data curation. **Elena Tchernychova:** Investigation, Data curation. **M. Pilar Lobera:** Writing – review & editing, Supervision. **Robert Dominko:** Writing – review & editing, Supervision, Funding acquisition. **María Bernechea:** Writing – review & editing, Supervision, Project administration, Funding acquisition, Conceptualization.

### Declaration of competing interest

The authors declare the following financial interests/personal relationships which may be considered as potential competing interests:

Maria Bernechea reports financial support was provided by MCIN, AEI. Maria Bernechea reports financial support was provided by CIBER-BBN. Maria Bernechea reports financial support was provided by ICTS NANBIOSIS. Maria Bernechea reports equipment, drugs, or supplies was provided by ICTS ELECMi node Laboratorio de Microscopias Avanzadas. Maria Bernechea reports equipment, drugs, or supplies was provided by Servicio General de Apoyo a la Investigación-SAI, Universidad de Zaragoza. Robert Dominko reports financial support was provided by Slovenian Research and Innovation Agency (ARIS). Maria Bernechea reports financial support was provided by ERA.NET network. If there are other authors, they declare that they have no known competing financial interests or personal relationships that could have appeared to influence the work reported in this paper.

### Data availability

Data will be made available on request.

### Acknowledgement

Authors acknowledge ERA.NET network for funding NOEL project, SA, MPL and MB acknowledge MCIN/AEI/10.13039/501100011033 (Ref: PRTR-C17.II with funding from European Union NextGenerationEU, promoted by the Government of Aragon, and PCI2019–10363), CIBER-BBN, ICTS “NANBIOSIS”, instrumentation and technical advice provided by the National Facility ICTS ELECMi node “Laboratorio de Microscopias Avanzadas”, and Servicio General de Apoyo a la Investigación-SAI, Universidad de Zaragoza. BT, AV and RD further acknowledge financial support from the Slovenian Research and Innovation Agency (ARIS), research core funding P2-0423 and project N2-0266.

### Appendix A. Supplementary data

Supplementary data to this article can be found online at <https://doi.org/10.1016/j.jpowsour.2024.234730>.

### References

- [1] K.M. Tan, T.S. Babu, V.K. Ramachandaramurthy, P. Kasinathan, S.G. Solanki, S. K. Raveendran, Empowering smart grid: a comprehensive review of energy storage technology and application with renewable energy integration, *J. Energy Storage* 39 (2021) 102591, <https://doi.org/10.1016/j.est.2021.102591>.
- [2] J.M. Tarascon, M. Armand, Issues and challenges facing rechargeable lithium batteries, *Nature* 414 (2001) 359–367, <https://doi.org/10.1038/35104644>.
- [3] R. Xiong, Y. Pan, W. Shen, H. Li, F. Sun, Lithium-ion battery aging mechanisms and diagnosis method for automotive applications: recent advances and perspectives, *Renew. Sustain. Energy Rev.* 131 (2020) 110048, <https://doi.org/10.1016/j.rser.2020.110048>.
- [4] Y. Yang, E.G. Okonkwo, G. Huang, S. Xu, W. Sun, Y. He, On the sustainability of lithium ion battery industry – a review and perspective, *Energy Storage Mater.* 36 (2021) 186–212, <https://doi.org/10.1016/j.ensm.2020.12.019>.
- [5] H. Moriwake, A. Kuwabara, C.A.J. Fisher, Y. Ikuhara, Why is sodium-intercalated graphite unstable? *RSC Adv.* 7 (2017) 36550–36554, <https://doi.org/10.1039/c7ra06777a>.
- [6] K. Wu, X. Dou, X. Zhang, C. Ouyang, The sodium-ion battery: an energy-storage technology for a carbon-neutral world, *Engineering* 21 (2023) 36–38, <https://doi.org/10.1016/j.eng.2022.04.011>.
- [7] S. Sarkar, S. Roy, Y. Hou, S. Sun, J. Zhang, Y. Zhao, Recent progress in amorphous carbon-based materials for anodes of sodium-ion batteries: synthesis strategies, mechanisms, and performance, *ChemSusChem* 14 (2021) 3693–3723, <https://doi.org/10.1002/cssc.202101270>.
- [8] X. Dou, I. Hasa, D. Saurel, C. Vaalma, L. Wu, D. Buchholz, D. Bresser, S. Komaba, S. Passerini, Hard carbons for sodium-ion batteries: structure, analysis, sustainability, and electrochemistry, *Mater. Today* 23 (2019) 87–104, <https://doi.org/10.1016/j.mattod.2018.12.040>.
- [9] R. Zhao, N. Sun, B. Xu, Recent advances in heterostructured carbon materials as anodes for sodium-ion batteries, *Small Struct.* 2 (2021) 2100132, <https://doi.org/10.1002/ssr.202100132>.
- [10] Y. Zhen, Y. Chen, F. Li, Z. Guo, Z. Hong, M.-M. Titirici, Ultrafast synthesis of hard carbon anodes for sodium-ion batteries, *Proc. Natl. Acad. Sci. USA* 118 (2021) e211119118, <https://doi.org/10.1073/pnas.2111191118>.
- [11] I. El Moctar, Q. Ni, Y. Bai, F. Wu, C. Wu, Hard carbon anode materials for sodium-ion batteries, *Functional Materials Letters* 11 (2018) 1830003, <https://doi.org/10.1142/S1793604718300037>.
- [12] Z. Jian, C. Bommier, L. Luo, Z. Li, W. Wang, C. Wang, P.A. Greaney, X. Ji, Insights on the mechanism of Na-ion storage in soft carbon anode, *Chem. Mater.* 29 (2017) 2314–2320, <https://doi.org/10.1021/acs.chemmater.6b05474>.
- [13] E. Peled, The electrochemical behavior of alkali and alkaline earth metals in nonaqueous battery systems—the solid electrolyte interphase model, *J. Electrochem. Soc.* 126 (1979) 2047, <https://doi.org/10.1149/1.2128859>.
- [14] E. Peled, D. Golodnitsky, G. Ardel, Advanced model for solid electrolyte interphase electrodes in liquid and polymer electrolytes, *J. Electrochem. Soc.* 144 (1997) L208, <https://doi.org/10.1149/1.1837858>.
- [15] X. Yu, A. Manthiram, Electrode-electrolyte interfaces in lithium-based batteries, *Energy Environ. Sci.* 11 (2018) 527–543, <https://doi.org/10.1039/c7ee02555f>.
- [16] J. Fondard, E. Irisarri, C. Courrèges, M.R. Palacin, A. Ponrouch, R. Dedryvère, SEI composition on hard carbon in Na-ion batteries after long cycling: influence of salts (NaPF<sub>6</sub>, NaTFSI) and additives (PEC, DMCF), *J. Electrochem. Soc.* 167 (2020) 070526, <https://doi.org/10.1149/1945-7111/ab75fd>.
- [17] M. Liu, F. Wu, Y. Gong, Y. Li, Y. Li, X. Feng, Q. Li, C. Wu, Y. Bai, Interfacial-catalysis-enabled layered and inorganic-rich SEI on hard carbon anodes in ester electrolytes for sodium-ion batteries, *Adv. Mater.* 35 (2023) 2300002, <https://doi.org/10.1002/adma.202300002>.
- [18] J. Collins, G. Gourdin, M. Foster, D. Qu, Carbon surface functionalities and SEI formation during Li intercalation, *Carbon* 92 (2015) 193–244, <https://doi.org/10.1016/j.carbon.2015.04.007>.
- [19] W. Guo, Y. Meng, Y. Hu, X. Wu, Z. Ju, Q. Zhuang, Surface and interface modification of electrode materials for lithium-ion batteries with organic liquid electrolyte, *Front. Energy Res.* 8 (2020) 170, <https://doi.org/10.3389/fenrg.2020.00170>.
- [20] A. Ponrouch, D. Monti, A. Boschin, B. Steen, P. Johansson, M.R. Palacin, Non-aqueous electrolytes for sodium-ion batteries, *J. Mater. Chem. A* 3 (2015) 22–42, <https://doi.org/10.1039/C4TA04428B>.
- [21] Y. Zhen, R. Sa, K. Zhou, L. Ding, Y. Chen, S. Mathur, Z. Hong, Breaking the limitation of sodium-ion storage for nanostructured carbon anode by engineering desolvation barrier with neat electrolytes, *Nano Energy* 74 (2020) 104895, <https://doi.org/10.1016/j.nanoen.2020.104895>.
- [22] R. Mogensen, D. Brandell, R. Younesi, Solubility of the solid electrolyte interphase (SEI) in sodium ion batteries, *ACS Energy Lett.* 1 (2016) 1173–1178, <https://doi.org/10.1021/acsenerylett.6b00491>.
- [23] H. Xie, Z. Wu, Z. Wang, N. Qin, Y. Li, Y. Cao, Z. Lu, Solid electrolyte interface stabilization via surface oxygen species functionalization in hard carbon for superior performance sodium-ion batteries, *J. Mater. Chem. A* 8 (2020) 3606–3612, <https://doi.org/10.1039/c9ta12429b>.
- [24] H. Sopha, G.D. Salián, R. Zazpe, J. Prikryl, L. Hromadko, T. Djenizian, J.M. Macak, ALD Al<sub>2</sub>O<sub>3</sub>-coated TiO<sub>2</sub> nanotube layers as anodes for lithium-ion batteries, *ACS Omega* 2 (2017) 2749–2756, <https://doi.org/10.1021/acsomega.7b00463>.
- [25] X.X. He, J.H. Zhao, W.H. Lai, R. Li, Z. Yang, C.M. Xu, Y. Dai, Y. Gao, X.H. Liu, L. Li, G. Xu, Y. Qiao, S.L. Chou, M. Wu, Soft-carbon-coated, free-standing, low-defect, hard-carbon anode to achieve a 94% initial coulombic efficiency for sodium-ion batteries, *ACS Appl. Mater. Interfaces* 13 (2021) 44358–44368, <https://doi.org/10.1021/acsmi.1c12171>.
- [26] C. Wei, W. Dang, M. Li, X. Ma, M. Li, Y. Zhang, Hard-soft carbon nanocomposite prepared by pyrolyzing biomass and coal waste as sodium-ion batteries anode material, *Mater. Lett.* 330 (2023) 133368, <https://doi.org/10.1016/j.matlet.2022.133368>.
- [27] Z. Tang, S. Zhou, P. Wu, H. Wang, Y. Huang, Y. Zhang, D. Sun, Y. Tang, H. Wang, Engineering surface oxygenated functionalities on commercial hard carbon toward superior sodium storage, *Chem. Eng. J.* 441 (2022) 135899, <https://doi.org/10.1016/j.cej.2022.135899>.
- [28] L.A. Romero-Cano, H. García-Rosero, F. Carrasco-Marín, A.F. Pérez-Cadenas, L. V. González-Gutiérrez, A.I. Zárate-Guzmán, G. Ramos-Sánchez, Surface functionalization to abate the irreversible capacity of hard carbons derived from

- grapefruit peels for sodium-ion batteries, *Electrochim. Acta* 326 (2019) 134973, <https://doi.org/10.1016/j.electacta.2019.134973>.
- [29] C.-X. Yu, Y. Li, Z.-H. Wang, X.-R. Wang, Y. Bai, C. Wu, Surface engineering based on in situ electro-polymerization to boost the initial Coulombic efficiency of hard carbon anode for sodium-ion battery, *Rare Met.* 41 (2022) 1616–1625, <https://doi.org/10.1007/s12598>.
- [30] F.A. Soto, P. Yan, M.H. Engelhard, A. Marzouk, C. Wang, G. Xu, Z. Chen, K. Amine, J. Liu, V.L. Sprenkle, F. El-Mellouhi, P.B. Balbuena, X. Li, Tuning the solid electrolyte interphase for selective Li- and Na-ion storage in hard carbon, *Adv. Mater.* 29 (2017) 1606860, <https://doi.org/10.1002/adma.201606860>.
- [31] L.A. Ma, A.J. Naylor, L. Nyholm, R. Younesi, Strategies for mitigating dissolution of solid electrolyte interphases in sodium-ion batteries, *Angew. Chem. Int. Ed.* 60 (2021) 4855–4863, <https://doi.org/10.1002/anie.202103803>.
- [32] B. Sun, W. Zheng, S. Lou, B. Xie, C. Cui, G.X. Zhang, F. Kong, Y. Ma, C. Du, P. Zuo, J. Xie, G. Yin, Synergistically tailoring the electronic structure and ion diffusion of atomically thin Co(OH)<sub>2</sub> nanosheets enable fast pseudocapacitive sodium ion storage, *Adv. Funct. Mater.* 33 (2022) 2211711, <https://doi.org/10.1002/adfm.202211711>.
- [33] M. Ma, H. Cai, C. Xu, R. Huang, S. Wang, H. Pan, Y.S. Hu, Engineering solid electrolyte interface at nano-scale for high-performance hard carbon in sodium-ion batteries, *Adv. Funct. Mater.* 31 (2021) 2100278, <https://doi.org/10.1002/adfm.202100278>.
- [34] H. Wang, C. Zhu, J. Liu, S. Qi, M. Wu, J. Huang, D. Wu, J. Ma, Formation of NaF-rich solid electrolyte interphase on Na anode through additive-induced anion-enriched structure of Na<sup>+</sup> solvation, *Angew. Chem. Int. Ed.* 61 (2022) e202208506, <https://doi.org/10.1002/anie.202208506>.
- [35] M. Xu, Y. Li, M. Ihsan-Ul-Haq, N. Mubarak, Z. Liu, J. Wu, Z. Luo, J.K. Kim, NaF-rich solid electrolyte interphase for dendrite-free sodium metal batteries, *Energy Storage Mater.* 44 (2022) 477–486, <https://doi.org/10.1016/j.ensm.2021.10.038>.
- [36] Z.W. Seh, J. Sun, Y. Sun, Y. Cui, A highly reversible room-temperature sodium metal anode, *ACS Cent. Sci.* 1 (2015) 449–455, <https://doi.org/10.1021/acscentsci.5b00328>.
- [37] S. Singsen, F. Ospina-Acevedo, S. Suthirakun, P. Hirunsit, P.B. Balbuena, Role of inorganic layers on polysulfide decomposition at sodium-metal anode surfaces for room temperature Na/S batteries, *Phys. Chem. Chem. Phys.* 25 (2023) 26316–26326, <https://doi.org/10.1039/d3cp03048b>.
- [38] Y. Li, M. Liu, X. Feng, Y. Li, F. Wu, Y. Bai, C. Wu, How can the electrode influence the formation of the solid electrolyte interface? *ACS Energy Lett.* 6 (2021) 3307–3320, <https://doi.org/10.1021/acsenergylett.1c01359>.
- [39] A. Slesinski, S. Sroka, S. Aina, J. Piwek, K. Fic, M.P. Lobera, M. Bernechea, E. Frackowiak, A double-redox aqueous capacitor with high energy output, *J. Mater. Chem. A* 11 (2023) 6258–6273, <https://doi.org/10.1039/D2TA09541F>.
- [40] B. Tratnik, N. Van De Velde, I. Jerman, G. Kapun, E. Tchernychova, M. Tomšič, A. Jamnik, B. Genorio, A. Vizintin, R. Dominko, Correlating structural properties with electrochemical behavior of non-graphitizable carbons in Na-ion batteries, *ACS Appl. Energy Mater.* 5 (2022) 10667–10679, <https://doi.org/10.1021/acsaem.2c01390>.
- [41] C. Bommier, T.W. Surta, M. Dolgos, X. Ji, New mechanistic insights on Na-ion storage in nongraphitizable carbon, *Nano Lett.* 15 (2015) 5888–5892, <https://doi.org/10.1021/acs.nanolett.5b01969>.
- [42] J. Kim, S. Park, S. Hwang, W.S. Yoon, Principles and applications of galvanostatic intermittent titration technique for lithium-ion batteries, *J. Electrochem. Sci. Technol.* 13 (2022) 19–31, <https://doi.org/10.33961/jecst.2021.00836>.
- [43] J.P. Guzowski, E.J. Delaney, M.J. Humora, E. Irdam, W.F. Kiesman, A. Kwok, A. D. Moran, Understanding and control of dimethyl sulfate in a manufacturing process: kinetic modeling of a Fischer esterification catalyzed by H<sub>2</sub>SO<sub>4</sub>, *Org. Process, Res. Dev.* 16 (2012) 232–239, <https://doi.org/10.1021/op200323j>.
- [44] O. Onija, G. Borodi, I. Kacso, M.N. Pop, D. Dadarlat, I. Bratu, N. Jumate, Preparation and characterization of urea-oxalic acid solid form, *AIP Conf. Proc.* Vol. 1425 (2012) 35–38, <https://doi.org/10.1063/1.3681960>.
- [45] X. Huang, Q. Zhao, R.P. Young, X. Zhang, E.D. Walter, Y. Chen, E. Nakouzi, S. D. Taylor, J.S. Loring, Z. Wang, K.S. Hofmocker, K.M. Rosso, Photo-production of reactive oxygen species and degradation of dissolved organic matter by hematite nanoplates functionalized by adsorbed oxalate, *Environ. Sci.: Nano* 7 (2020) 2278–2292, <https://doi.org/10.1039/d0en00365d>.
- [46] K. Achelhi, S. Masse, G. Laurent, A. Saoiabi, A. Laghzizil, T. Coradin, Role of carboxylate chelating agents on the chemical, structural and textural properties of hydroxyapatite, *Dalton Trans.* 39 (2010) 10644–10651, <https://doi.org/10.1039/c0dt00251h>.
- [47] L. Shi, Q. Liu, X. Guo, W. Wu, Z. Liu, Pyrolysis behavior and bonding information of coal — a TGA study, *Fuel Process. Technol.* 108 (2013) 125–132, <https://doi.org/10.1016/j.fuproc.2012.06.023>.
- [48] J.A.L. Dos Santos, F. Baum, E.C. Kohlrausch, F.C. Tavares, T. Pretto, F.P. Dos Santos, J.F. Leite Santos, S. Khan, M.J. Leite Santos, 3-Mercaptopropionic, 4-mercaptobenzoic, and oleic acid-capped CdSe quantum dots: interparticle distance, anchoring groups, and surface passivation, *J. Nanomater.* 2019 (2019) 2796746, <https://doi.org/10.1155/2019/2796746>.
- [49] B. Lesiak, N. Rangam, P. Jiricek, I. Gordeev, J. Tóth, L. Kóvér, M. Mohai, P. Borowicz, Surface study of Fe<sub>3</sub>O<sub>4</sub> nanoparticles functionalized with biocompatible adsorbed molecules, *Front. Chem.* 7 (2019) 642, <https://doi.org/10.3389/fchem.2019.00642>.
- [50] A. Kirakosyan, D. Lee, Y. Choi, N. Jung, J. Choi, Poly(styrene sulfonic acid)-grafted carbon black synthesized by surface-initiated atom transfer radical polymerization, *Molecules* 28 (2023) 4168, <https://doi.org/10.3390/molecules28104168>.
- [51] L. Wan, S. Hu, J. Liu, D. Chen, S. Liu, R. Xiao, Y. Zhang, J. Chen, C. Du, M. Xie, Enhancing the energy density of supercapacitors by introducing nitrogen species into hierarchical porous carbon derived from camellia pollen, *Ionics* 26 (2020) 2549–2561, <https://doi.org/10.1007/s11581-019-03394-7>.
- [52] Z. Peng, H. Li, Q. Li, Y. Hu, Microwave-Assisted thiol-ene click chemistry of carbon nanofibers, *Colloids Surf. A Physicochem. Eng. Asp.* 533 (2017) 48–54, <https://doi.org/10.1016/j.colsurfa.2017.08.018>.
- [53] J.F. Moulder, W.F. Stickle, P.E. Sobol, K.D. Bomben, J. Chastain, *Handbook of X-Ray Photoelectron Spectroscopy A Reference Book of Standard Spectra for Identification and Interpretation of XPS Data*, 1992.
- [54] T. Yoon, N. Chapman, D.M. Seo, B.L. Lucht, Lithium salt effects on silicon electrode performance and solid electrolyte interphase (SEI) structure, role of solution structure on SEI formation, *J. Electrochem. Soc.* 164 (2017) A2082–A2088, <https://doi.org/10.1149/2.1421709jes>.
- [55] H. Shin, J. Park, A.M. Sastry, W. Lu, Effects of fluoroethylene carbonate (FEC) on anode and cathode interfaces at elevated temperatures, *J. Electrochem. Soc.* 162 (2015) A1683–A1692, <https://doi.org/10.1149/2.0071509jes>.
- [56] J.C. Burns, R. Petibon, K.J. Nelson, N.N. Sinha, A. Kassam, B.M. Way, J.R. Dahn, Studies of the effect of varying vinylene carbonate (VC) content in lithium ion cells on cycling performance and cell impedance, *J. Electrochem. Soc.* 160 (2013) A1668–A1674, <https://doi.org/10.1149/2.031310jes>.
- [57] L. El Ouatani, R. Dedryvère, C. Siret, P. Biensan, S. Reynaud, P. Iratçabal, D. Gonbeau, The effect of vinylene carbonate additive on surface film formation on both electrodes in Li-ion batteries, *J. Electrochem. Soc.* 156 (2009) A103, <https://doi.org/10.1149/1.3029674>.
- [58] Z. Liu, Z. Lu, S. Guo, Q.H. Yang, H. Zhou, Toward high performance anodes for sodium-ion batteries: from hard carbons to anode-free systems, *ACS Cent. Sci.* 9 (2023) 1076–1087, <https://doi.org/10.1021/acscentsci.3c00301>.
- [59] J. Yang, X. Wang, W. Dai, X. Lian, X. Cui, W. Zhang, K. Zhang, M. Lin, R. Zou, K. P. Loh, Q.H. Yang, W. Chen, From micropores to ultra-micropores inside hard carbon: toward enhanced capacity in room-/low-temperature sodium-ion storage, *Nano-Micro Lett.* 13 (2021) 98, <https://doi.org/10.1007/s40820-020-00587-y>.
- [60] Z. Hong, Y. Zhen, Y. Ruan, M. Kang, K. Zhou, J.M. Zhang, Z. Huang, M. Wei, Rational design and general synthesis of S-doped hard carbon with tunable doping sites toward excellent Na-ion storage performance, *Adv. Mater.* 30 (2018) 1802035, <https://doi.org/10.1002/adma.201802035>.
- [61] S. Huang, Y. Lv, W. Wen, T. Xue, P. Jia, J. Wang, J. Zhang, Y. Zhao, Three-dimensional hierarchical porous hard carbon for excellent sodium/potassium storage and mechanism investigation, *Mater. Today Energy* 20 (2021) 100673, <https://doi.org/10.1016/j.mtener.2021.100673>.
- [62] Y. Li, Y.S. Hu, M.M. Titirici, L. Chen, X. Huang, Hard carbon microtubes made from renewable cotton as high-performance anode material for sodium-ion batteries, *Adv. Energy Mater.* 6 (2016) 1600659, <https://doi.org/10.1002/aenm.201600659>.
- [63] G.G. Eshetu, T. Diemant, M. Hekmatfar, S. Grugeon, R.J. Behm, S. Laruelle, M. Armand, S. Passerini, Impact of the electrolyte salt anion on the solid electrolyte interphase formation in sodium ion batteries, *Nano Energy* 55 (2019) 327–340, <https://doi.org/10.1016/j.nanoen.2018.10.040>.
- [64] T. Nunney, R. White, Characterizing materials for energy generation using X-ray photoelectron spectroscopy (XPS), *Microscopy Today* 19 (2011) 22–28, <https://doi.org/10.1017/s1551929511000022>.
- [65] L. Ji, M. Gu, Y. Shao, X. Li, M.H. Engelhard, B.W. Arey, W. Wang, Z. Nie, J. Xiao, C. Wang, J.G. Zhang, J. Liu, Controlling SEI formation on SnSb-porous carbon nanofibers for improved Na ion storage, *Adv. Mater.* 26 (2014) 2901–2908, <https://doi.org/10.1002/adma.201304962>.
- [66] J. Schenk, D. Leistschneider, S. Hoepfner, U.S. Schubert, K. Schütjajew, M. Oschatz, Influence of structural modifications on the alkali ion storage properties of carbon black in hybrid ion capacitor negative electrodes, *Sustain. Energy Fuels* 7 (2023) 3871–3882, <https://doi.org/10.1039/d3se00642e>.